Broadband antireflective germanium surfaces based on subwavelength structures for photovoltaic cell applications

Jung Woo Leem,[1] Young Min Song,[2] and Jae Su Yu[1,*]

[1]*Department of Electronics and Radio Engineering, Kyung Hee University, 1 Seocheon-dong, Giheung-gu, Yongin-si, Gyeonggi-do 446-701, South Korea*

[2]*Department of Materials Science and Engineering, University of Illinois at Urbana-Champaign, Urbana, Illinois 61801, USA*

[*]*jsyu@khu.ac.kr*

Abstract: We fabricated the germanium (Ge) subwavelength structures (SWSs) using gold (Au) metallic nanopatterns dewetted by rapid thermal annealing and inductively coupled plasma etching in $SiCl_4$ plasma for Ge-based photovoltaic cells. Using the optimized Au nanopatterns as an etch mask, the Ge SWSs were formed by varying the etching parameters to achieve the better antireflection properties. The reflectance of Ge SWSs depended strongly on their period, height, and shape which are closely related to the refractive index profile between air and the Ge substrate. The tapered cone Ge SWSs reduced considerably the reflectance compared to the samples with a truncated cone shape as well as the Ge substrate due to the linearly graded refractive index distribution from air to the Ge substrate. The Ge SWS with the tapered cone shape and high height exhibited a dramatic decrease in the reflectance (i.e., <10%) over a wide wavelength region of 350-1800 nm, thus leading to a low solar weighted reflectance of ~3.6%. The reflectance was also lower than ~8.8% at a wavelength of 633 nm in the incident angle range of 15-85°. The measured reflectance data of Ge SWSs showed similar trends to the calculated results in a rigorous coupled wave analysis simulation.

OCIS codes: (050.6624) Subwavelength structures; (220.4241) Nanostructure fabrication; (310.1210) Antireflection coatings.

References and links

1. R. Kaufmann, G. Isella, A. Sanchez-Amores, S. Neukom, A. Neels, L. Neumann, A. Brenzikofer, A. Dommann, C. Urban, and H. von Känel, "Near infrared image sensor with integrated germanium photodiodes," J. Appl. Phys. **110**(2), 023107 (2011).
2. L. Tang, S. E. Kocabas, S. Latif, A. K. Okyay, D. S. Ly-Gagnon, K. C. Saraswat, and D. A. B. Miller, "Nanometre-scale germanium photodetector enhanced by a near-infrared dipole antenna," Nat. Photonics **2**(4), 226–229 (2008).
3. W. Guter, J. Schöne, S. P. Philipps, M. Steiner, G. Siefer, A. Wekkeli, E. Welser, E. Oliva, A. W. Bett, and F. Dimroth, "Current-matched triple-junction solar cell reaching 41.1% conversion efficiency under concentrated sunlight," Appl. Phys. Lett. **94**(22), 223504 (2009).
4. M. Yamaguchi, T. Takamoto, and K. Araki, "Super high-efficiency multi-junction and concentrator solar cells," Sol. Energy Mater. Sol. Cells **90**(18-19), 3068–3077 (2006).
5. I. Prieto, B. Galiana, P. A. Postigo, C. Algora, L. J. Martínez, and I. Rey-Stolle, "Enhanced quantum efficiency of Ge solar cells by a two-dimensional photonic crystal nanostructured surface," Appl. Phys. Lett. **94**(19), 191102 (2009).
6. N. E. Posthuma, J. van der Heide, G. Flamand, and J. Poortmans, "Emitter formation and contact realization by diffusion for germanium photovoltaic devices," IEEE Trans. Electron. Dev. **54**(5), 1210–1215 (2007).
7. N. E. Posthuma, J. van der Heide, G. Flamand, and J. Poortmans, "Development of low cost germanium photovoltaic cells for application in TPV using spin on diffusants," AIP Conf. Proc. **738**, 337–344 (2004).
8. T. Nagashima, K. Okumura, and M. Yamaguchi, "A germanium back contact type thermophotovoltaic cell," AIP Conf. Proc. **890**, 174–181 (2007).

#155555 - $15.00 USD Received 28 Sep 2011; revised 13 Nov 2011; accepted 23 Nov 2011; published 9 Dec 2011

9. J. van der Heide, N. E. Posthuma, G. Flamand, W. Geens, and J. Poortmans, "Cost-efficient thermophotovoltaic cells based on germanium substrates," Sol. Energy Mater. Sol. Cells **93**(10), 1810–1816 (2009).
10. P. Yu, C. H. Chang, C. H. Chiu, C. S. Yang, J. C. Yu, H. C. Kuo, S. H. Hsu, and Y. C. Chang, "Efficiency enhancement of GaAs photovoltaics employing antireflective indium tin oxide nanocolumns," Adv. Mater. **21**(16), 1618–1621 (2009).
11. Y. J. Lee, D. S. Ruby, D. W. Peters, B. B. McKenzie, and J. W. P. Hsu, "ZnO nanostructures as efficient antireflection layers in solar cells," Nano Lett. **8**(5), 1501–1505 (2008).
12. T. Hanrath and B. A. Korgel, "Chemical surface passivation of Ge nanowires," J. Am. Chem. Soc. **126**(47), 15466–15472 (2004).
13. Y. Dan, K. Seo, K. Takei, J. H. Meza, A. Javey, and K. B. Crozier, "Dramatic reduction of surface recombination by in situ surface passivation of silicon nanowires," Nano Lett. **11**(6), 2527–2532 (2011).
14. P. B. Clapham and M. C. Hutley, "Reduction of lens reflexion by the "Moth Eye" principle," Nature **244**(5414), 281–282 (1973).
15. Y. M. Song, S. J. Jang, J. S. Yu, and Y. T. Lee, "Bioinspired parabola subwavelength structures for improved broadband antireflection," Small **6**(9), 984–987 (2010).
16. M. Y. Chiu, C. H. Chang, M. A. Tsai, F. Y. Chang, and P. Yu, "Improved optical transmission and current matching of a triple-junction solar cell utilizing sub-wavelength structures," Opt. Express **18**(S3 Suppl 3), A308–A313 (2010).
17. E. S. Choi, Y. M. Song, G. C. Park, and Y. T. Lee, "Disordered antireflective subwavelength structures using Ag nanoparticles for GaN-based optical device applications," J. Nanosci. Nanotechnol. **11**(2), 1342–1345 (2011).
18. K. C. Sahoo, Y. Li, and E. Y. Chang, "Shape effect of silicon nitride subwavelength structure on reflectance for silicon solar cells," IEEE Trans. Electron. Dev. **57**(10), 2427–2433 (2010).
19. J. W. Leem, Y. M. Song, Y. T. Lee, and J. S. Yu, "Antireflective properties of AZO subwavelength gratings patterned by holographic lithography," Appl. Phys. B **99**(4), 695–700 (2010).
20. B. J. Kim and J. Kim, "Fabrication of GaAs subwavelength structure (SWS) for solar cell applications," Opt. Express **19**(S3 Suppl 3), A326–A330 (2011).
21. J. W. Leem, D. H. Joo, and J. S. Yu, "Biomimetic parabola-shaped AZO subwavelength grating structures for efficient antireflection of Si-based solar cells," Sol. Energy Mater. Sol. Cells **95**(8), 2221–2227 (2011).
22. J. M. Lee and B. I. Kim, "Thermal dewetting of Pt thin film: Etch-masks for the fabrication of semiconductor nanostructures," Mater. Sci. Eng. A **449–451**, 769–773 (2007).
23. S. Wang, X. Z. Yu, and H. T. Fan, "Simple lithographic approach for subwavelength structure antireflection," Appl. Phys. Lett. **91**(6), 061105 (2007).
24. C. H. Chiu, P. Yu, H. C. Kuo, C. C. Chen, T. C. Lu, S. C. Wang, S. H. Hsu, Y. J. Cheng, and Y. C. Chang, "Broadband and omnidirectional antireflection employing disordered GaN nanopillars," Opt. Express **16**(12), 8748–8754 (2008).
25. J. W. Leem, J. S. Yu, Y. M. Song, and Y. T. Lee, "Antireflection characteristics of disordered GaAs subwavelength structures by thermally dewetted Au nanoparticles," Sol. Energy Mater. Sol. Cells **95**(2), 669–676 (2011).
26. Y. Li, J. Zhang, and B. Yang, "Antireflection surfaces based on biomimetic nanopillared arrays," Nano Today **5**(2), 117–127 (2010).
27. J. Zhu, C. M. Hsu, Z. Yu, S. Fan, and Y. Cui, "Nanodome solar cells with efficient light management and self-cleaning," Nano Lett. **10**(6), 1979–1984 (2010).
28. A. J. Jääskeläinen, K. E. Peiponen, J. Räty, U. Tapper, O. Richard, E. I. Kauppinen, and K. Lumme, "Estimation of the refractive index of plastic pigments by Wiener bounds," Opt. Eng. **39**(11), 2959–2963 (2000).
29. D. G. Stavenga, S. Foletti, G. Palasantzas, and K. Arikawa, "Light on the moth-eye corneal nipple array of butterflies," Proc. Biol. Sci. **273**(1587), 661–667 (2006).
30. M. G. Moharam and T. K. Gaylord, "Rigorous coupled-wave analysis of planar-grating diffraction," J. Opt. Soc. Am. **71**(7), 811–818 (1981).
31. S. A. Boden and D. M. Bagnall, "Tunable reflection minima of nanostructured antireflective surfaces," Appl. Phys. Lett. **93**(13), 133108 (2008).
32. M. L. Kuo, D. J. Poxson, Y. S. Kim, F. W. Mont, J. K. Kim, E. F. Schubert, and S. Y. Lin, "Realization of a near-perfect antireflection coating for silicon solar energy utilization," Opt. Lett. **33**(21), 2527–2529 (2008).
33. D. J. Economou, "Modeling and simulation of plasma etching reactors for microelectronics," Thin Solid Films **365**(2), 348–367 (2000).
34. D. Redfield, "Method for evaluation of antireflection coatings," Solar Cells **3**(1), 27–33 (1981).

1. Introduction

Germanium (Ge), which has a relatively high charge-carrier mobility and high absorption coefficient, is one of the most useful semiconductor materials in optical and optoelectronic device applications such as image sensors, photodetectors, and solar cells [1–3]. Furthermore, the low energy bandgap (0.66 eV) of Ge allows for absorbing the photons in a wide wavelength range up to ~1800 nm. In solar cells, especially, the Ge is usually used as the substrate and bottom cell of monolithic tandem multi-junction solar cells as well as stand-

#155555 - $15.00 USD Received 28 Sep 2011; revised 13 Nov 2011; accepted 23 Nov 2011; published 9 Dec 2011

alone cells in hybrid lighting systems [4–7]. Also, Ge single-junction solar cells can be employed as a receiver in thermophotovoltaic systems, where a narrow-band radiation spectrum (i.e., a wavelength range of 1500-1600 nm) originated from a heat source is used [8,9]. However, the surface reflectivity of Ge is very high (i.e., >35%) due to the Fresnel reflection caused by its high refractive index. Thus, for practical device applications, efficient antireflection coatings (ARCs) are required to enhance the light absorption by suppressing Fresnel reflection losses. Various kinds of semiconductor nanostructures such as nanowires and nanorods were demonstrated for ARCs [10,11]. Unfortunately, these nanostructures lead to the larger surface recombination losses caused by the increased surface area, which may degrade the performance of devices. However, these losses can be somewhat reduced by a proper surface passivation of nanostructures [12,13]. Recently, subwavelength structures (SWSs) inspired by the moth-eye effect [14] have been widely studied as an alternative of the conventional thin film ARCs because they can efficiently reduce the surface reflection in the wide ranges of wavelength and incident angle [15–21].

Meanwhile, the thermal dewetting of thin metal films is one of useful and simple processes for high-density self-assembled metal nanoparticles over a large area, which can form the etch mask for dry etching in the nanostructure fabrication [22–25]. To achieve a good light absorption for solar cell applications, the geometric shape, size, and height of surface structures should be optimized [26,27]. Although studies on antireflective nanostructures of various materials such as silicon, indium tin oxide, silicon nitride, gallium nitride, and gallium arsenide were reported [17,18,23–25], there has been very little work on the Ge. In this work, we studied systematically the fabrication and characteristics of the Ge SWSs by inductively coupled plasma (ICP) etching using gold (Au) nanoparticles as an etch mask to form various surface profiles, with theoretical investigations using the rigorous coupled wave analysis (RCWA) simulation. The influence of the incident angle of light on the reflectance and solar weighted reflectance was also explored for solar cell applications.

2. Experimental details

Figure 1 shows the schematic diagram of the process steps for the fabrication of SWSs on Ge substrates using Au nanomask patterns. The top-view SEM images of thermally dewetted Au nanoparticles by rapid thermal annealing (RTA) process for Au film thicknesses of 5, 10, and 15 nm, respectively, and the refractive index profile of truncated and tapered cone Ge SWSs are also shown. Before cutting into substrate pieces with a size of ~1.7 × 1.7 cm^2, 2 inch p-type (100) Ge wafers were cleaned by acetone and methanol, rinsed in de-ionized water, and subsequently dried in a flowing nitrogen gas. To fabricate the etch nanomask patterns, first, the Au films of different thicknesses were directly deposited on Ge substrates by using a thermal evaporator (KVE-T2000, Korea Vac. Tech. Ltd.) under a background pressure of 2 × 10^{-6} Torr at room temperature. The thicknesses of Au films were 5, 10, and 15 nm. The deposition rate was set to ~0.5 Å/s as monitored by a quartz crystal oscillator. To achieve the desirable Au etch nanomask patterns, the samples were thermally dewetted by using a RTA system (KVR-2000, Korea Vac. Tech. Ltd.) at a temperature of 450 °C for 2 min in nitrogen environment. From the SEM images in Fig. 1, the Au films turned into rounded lens-like nanoparticles. This phenomenon is because the surface energy of metal films exceeds the sum of the surface energy of the semiconductor substrate and the interfacial energy between two layers [22]. Clearly, the average size and period of Au nanoparticles can be roughly controlled by the RTA condition as well as the Au film thickness. The average diameter and correlation distance of the disorderly patterned Au nanoparticles were estimated using a commercial image processor (ImageJ 1.42q, NIH), thus exhibiting approximately 57.1 ± 29, 132.5 ± 70, and 237.8 ± 100 nm and 110, 245, and 430 nm for Au film thicknesses of 5, 10, and 15 nm, respectively. Using the Au nanopatterns as the etch mask, the SWSs were fabricated on Ge substrates by an ICP (Plasmalab System 100, Oxford) etching process. The etching conditions (i.e., RF power, additional ICP power, process pressure, and etching time)

#155555 - $15.00 USD Received 28 Sep 2011; revised 13 Nov 2011; accepted 23 Nov 2011; published 9 Dec 2011

were changed to obtain a desirable etched profile of antireflective Ge surface structures. The thickness of Au films was very thin and the Au nanomask patterns were considerably removed during the ICP etching process. Particularly, for cone-shaped Ge SWSs, the Au nanomask patterns were almost removed. Nevertheless, the remaining Au nanopatterns after the etching were eliminated by Au etchant solution. As shown in the refractive index profile of Fig. 1, the effective refractive index is gradually varied from air (n_{air} = 1) to the Ge substrate (average n_{Ge}~4.8 at wavelengths of 350-1800 nm) via Ge SWSs, which is correlated with their effective volume fraction [23,28]. The refractive index of truncated cone Ge SWSs is abruptly changed at the interface of air/Ge SWSs, whereas the tapered cone Ge SWSs have a linear refractive index change from air to the Ge substrate. These different index profiles would modify the surface reflection properties [21,29]. The structural shape and morphology of the fabricated Ge SWSs were observed by using a scanning electron microscope (SEM, LEO SUPRA 55, Carl Zeiss) with an accelerating voltage of 10 kV. The total reflectance was measured by using UV-vis-NIR spectrophotometer (Cary 5000, Varian) with an integrating sphere at near-normal incidence angle of 8°. For angle-dependent reflectance measurements, the spectroscopic ellipsometry (V-VASE, J. A. Woollam Co. Inc.) was used at angles of 15-85° for linearly polarized light incidence in specular mode.

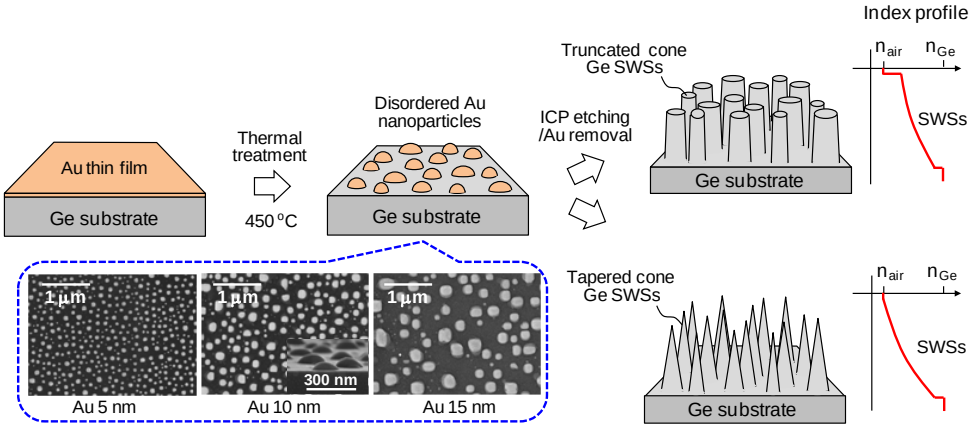

Fig. 1. Schematic diagram of the process steps for the fabrication of SWSs on Ge substrates using Au nanomask patterns. The tow-view SEM images of thermally dewetted Au nanoparticles and the refractive index profile of truncated and cone-shaped Ge SWSs are also shown.

3. Results and discussion

Figure 2(a) shows the 30°-tilted oblique-view SEM images of the etched Ge SWSs using Au nanomask patterns for Au film thicknesses of (i) 5 nm, (ii) 10 nm, and (iii) 15 nm. The corresponding cross-sectional SEM images are shown in the insets. The samples were etched with 50 RF power at 5 mTorr for 10 min in 5 sccm $SiCl_4$ plasma. It can be evidently observed that the Au nanopatterns were transferred directly onto the Ge substrates by the ICP etching, which results in Ge SWSs, as can be seen in Figs. 1 and 2. As the Au film thickness was increased from 5 to 15 nm, the Ge SWSs were changed from the truncated cone nanopillars to the cylindrical ones while their average height had similar values of about 107 ± 8 nm. This can be explained by the fact that the thinner Au nanoparticles with a small size (i.e., for 5 nm Au films) are more quickly removed at the edge of nanoparticles compared to the thicker and larger ones. In the etched Ge SWGs, the volume fraction ratios (i.e., the ratio of the volume occupied by the constituent semiconductor material to the total volume), which were roughly estimated from the SEM images with the help of the image processor, were approximately

#155555 - $15.00 USD Received 28 Sep 2011; revised 13 Nov 2011; accepted 23 Nov 2011; published 9 Dec 2011

0.7, 0.55, and 0.49 for 5, 10, and 15 nm of Au films, respectively. The theoretical analysis on the antireflective characteristics of the fabricated Ge SWSs was carried out using the RCWA simulation [30]. In calculations, the 5th order diffraction was used to obtain the diffraction efficiency of Ge SWSs, which is a sufficient number to stabilize the results numerically, and the incident light entered from air into the Ge SWS at normal incidence. Figure 2(b) shows the contour plot of the variation of calculated reflectance spectra as a function of the period of Ge SWSs. The three-dimensional simulation model used in this calculation, which is shown in the inset of Fig. 2(b), was constructed by the mean shape of the SEM image, assuming the truncated cones with a height of 110 nm and the six-fold hexagonal symmetry structure for simplicity. The apex diameter was set to 0.5 of the bottom diameter in the truncated cone. In calculations, the diameter of nanopillars was increased to the ratio value of 0.55 to the period of Ge SWSs in consideration of average diameter and correlation distance of the disorderly patterned Au nanoparticles. As the period of Ge SWSs is increased, the low reflectance band is shifted to the longer wavelength region [31]. However, the reflectance becomes higher at periods above 400 nm in the wavelength region of >600 nm. At periods around 250 nm, the reflectance of <10% is maintained in the wavelength range of 350-700 nm, as can be seen in Fig. 2(b). The electric field intensity distribution of the Ge SWS with a period of 250 nm at a wavelength of 1000 nm at normal incidence used in the calculation of Fig. 2(b) is shown in Fig. 2(c). The electric field is absorbed at the relatively short optical distance in the Ge due to its absorption.

Figure 2(d) shows the measured reflectance spectra of the corresponding Ge SWSs. The reflectance of Ge substrate is also shown for comparison. Due to the large difference in refractive index between air and the Ge, the surface reflectivity of Ge substrate was higher than 35% at wavelengths of 350-1800 nm. For the etched Ge SWSs, the reflectance is lower than that of the Ge substrate due to the gradual index change from air to the Ge substrate via Ge SWSs as displayed in Fig. 1. Above $\lambda \sim 1800$ nm, the abrupt increase in reflectance spectra is attributed to the backscattered light from the back surface of the Ge substrate since the Ge is transparent below its energy bandgap [32]. For Au nanopatterns of the 5 nm film, the reflectance of the Ge SWS is lower than that of other samples in the short wavelength range of 500-650 nm. In contrast, the low reflectance wavelength region was approximately 650-1000 nm for Au nanopatterns of the 10 nm film. This means that the low reflectance band is shifted towards the longer wavelength region as the average period of SWSs is increased. For the Ge SWS etched using Au nanopatterns of the 15 nm film, the reflectance spectrum had a similar shape over a wide wavelength region of 350-1800 nm, keeping the lower reflectance values. This results from the lower average height and longer average period of SWSs [31], closer to the flat substrate. Although there are some discrepancies between the measured and calculated results due to the simplicity of the geometric simulation model for the actually fabricated structures, the overall trend appears to be similar. Therefore, for Au nanomask patterns, the film thickness of 10 nm was chosen in this experiment because it provides a relatively low reflectance over a broad wavelength range of 650-1800 nm.

#155555 - $15.00 USD Received 28 Sep 2011; revised 13 Nov 2011; accepted 23 Nov 2011; published 9 Dec 2011

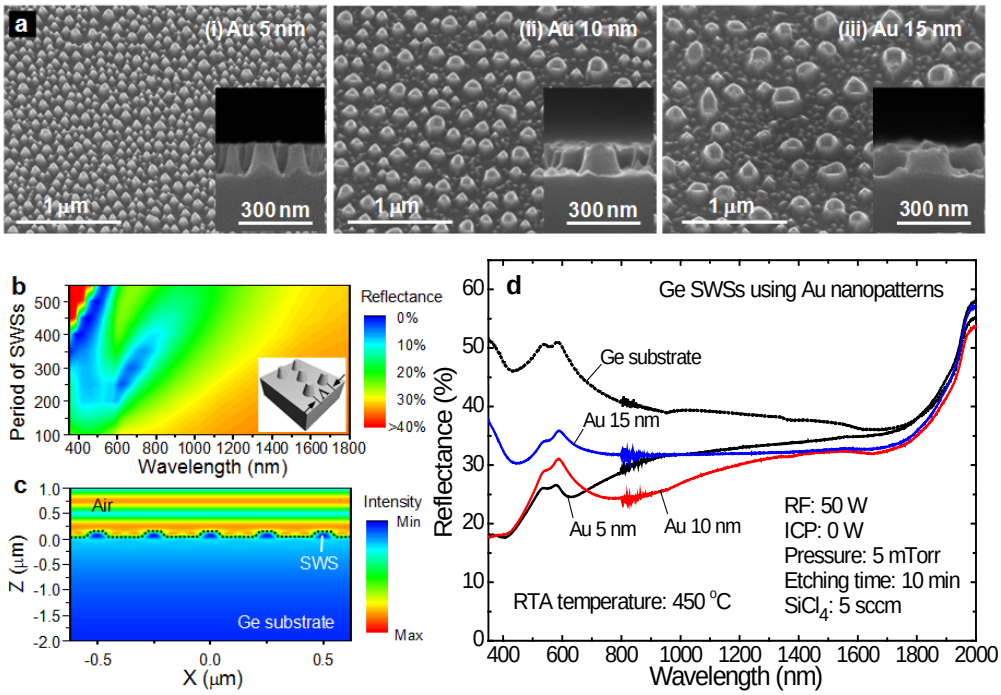

Fig. 2. (a) SEM images of etched Ge SWSs using Au nanomask patterns for Au film thicknesses of (i) 5 nm, (ii) 10 nm, and (iii) 15 nm, (b) contour plot of the variation of calculated reflectance spectra as a function of the period of Ge SWSs, (c) electric field intensity distribution of the Ge SWS at a wavelength of 1000 nm at normal incidence, and (d) measured reflectance spectra of the corresponding Ge SWSs.

Figure 3 shows (a) 10°-tilted side-view SEM images and (b) measured reflectance spectra of the etched Ge SWSs using Au nanomask patterns for RF powers of (i) 25 W, (ii) 50 W, (iii) 75 W, and (iv) 100 W. The process pressure and etching time were 5 mTorr and 10 min, respectively. As the RF power was increased from 25 to 100 W, the etching rate was increased from 8.3 to 20 nm/min owing to the increased ion energy flux, and the height of Ge SWSs became higher from 83±6 to 200±14 nm while their volume fraction ratio was decreased from ~0.58 to ~0.5. The shape of etched structures was also dependent on the RF power. The nanopillars in Ge SWSs were more tapered with increasing the RF power because the Au nanomask patterns were more quickly eroded from the edges due to the high RF power during the etching process. These tapered nanopillars with a cone shape in SWSs have a linearly graded refractive index profile, which results in the lower reflectance over a wide wavelength region than that of the cylindrical shaped SWSs [18]. As expected, at an RF power of 100 W, the more tapered Ge SWS with taller nanopillars exhibited a relatively low reflectance as shown in Fig. 3(b), leading to an average reflectance of ~16.7% at wavelengths of 350-1800 nm.

#155555 - $15.00 USD Received 28 Sep 2011; revised 13 Nov 2011; accepted 23 Nov 2011; published 9 Dec 2011

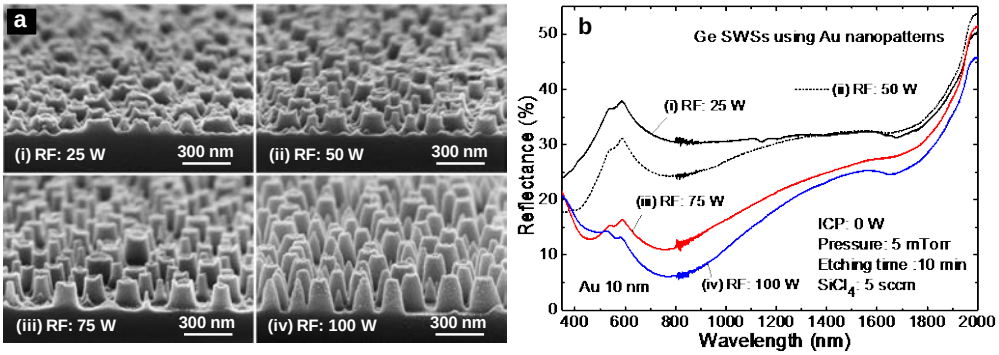

Fig. 3. (a) 10°-tilted side-view SEM images and (b) measured reflectance spectra of the etched Ge SWSs using Au nanomask patterns for RF powers of (i) 25 W, (ii) 50 W, (iii) 75 W, and (iv) 100 W.

Figure 4 shows the measured reflectance spectra of the etched Ge SWSs using Au nanomask patterns at different (a) additional ICP powers and (b) process pressures. The SEM images of the corresponding structures are shown in the insets. The etching process was carried out with 50W RF power for 10 min in 5 sccm $SiCl_4$ plasma. An additional ICP power enhances the etching of Au nanomask patterns as well as the Ge, which creates the nanopillars with a tapered shape. As the additional ICP power to 50 W RF power was raised from 50 to 100 W, the height of the etched Ge SWSs was increased from 348 ± 105 to 371 ± 166 nm, which decreased the reflectance as can be seen in Fig. 4(a). At a high additional ICP power of 100 W, the volume fraction ratio of tapered nanopillars in the SWS was ~0.62, which was larger than ~0.31 at 50 W. Their average height was slightly increased in spite of double the ICP power as shown in the SEM image of Fig. 4(a). It is noted that the etch selectivity of Ge over Au nanoparticle is decreased at higher ICP power. The volume fraction of nanopillars in SWSs affects the profile of effective refractive index between the Ge and air [21]. As shown in the SEM images of Fig. 4(b), the etched shape of Ge SWSs also relied strongly on the process pressure. As the process pressure was increased from 2 to 10 mTorr, the average etch rate of Ge SWSs was decreased from ~63.2 to ~12.8 nm/min. The volume fraction ratios were ~0.44 and ~0.54 at 2 and 10 mTorr, respectively. Their shape was changed from the tapered cone nanopillars with a high height at 2 mTorr to the truncated ones with a low height at 10 mTorr, particularly related to the variation of refractive index profile at the interface of air and Ge SWSs, as can be seen in Fig. 1. This is the reason why a relatively low process pressure reduces ion collisions due to the lower plasma density, which leads to higher ion kinetic energy and enhances the etch rate [33]. On the other hand, at a high pressure of 10 mTorr, the etching of Ge and Au nanopatterns was disturbed because of the ion scattering. During the etching process, the RF power with an additional 50 W ICP power was kept at 50 W. For the Ge SWS with the taller and tapered cone-shaped nanopillars at 2 mTorr, the average reflectance of 9.7% was lower than 26.1% of the truncated cone-shaped Ge SWS at 10 mTorr in the wavelength region of 350-1800 nm, exhibiting the SWS height of 632±150 nm (i.e., 128±10 nm at 10 mTorr). Thus, the height and shape of nanopillars in Ge SWSs can be controlled easily by adjusting the process pressure during the ICP etching procedure.

#155555 - $15.00 USD Received 28 Sep 2011; revised 13 Nov 2011; accepted 23 Nov 2011; published 9 Dec 2011

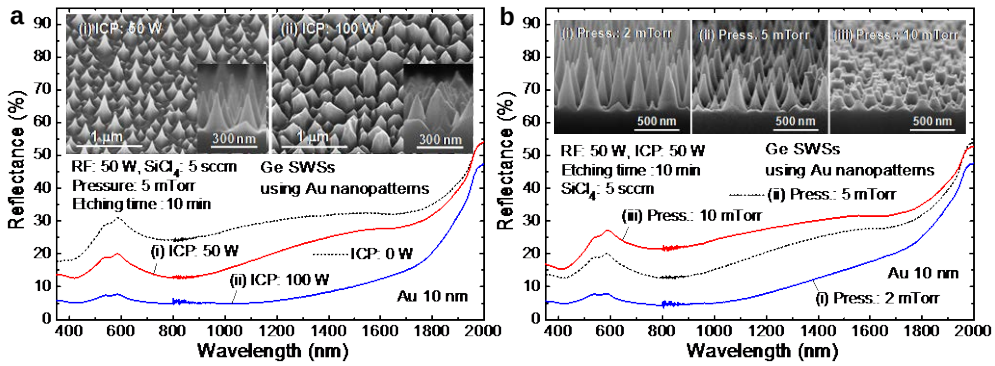

Fig. 4. Measured reflectance spectra of the etched Ge SWSs using Au nanomask patterns at different (a) additional ICP powers and (b) process pressures. The insets show the SEM images of the corresponding structures.

Figure 5(a) shows the 30°-tilted oblique-view SEM images of the etched Ge SWSs at etching times of (i) 5 min, (ii) 10 min, and (iii) 15 min using the Au nanomask patterns. The measured reflectance spectra of the corresponding structures are also shown in (iv) of Fig. 5(a). The samples were etched with 50 W RF power and 50 W additional ICP power at 2 mTorr in 5 sccm $SiCl_4$ plasma. The Au nanopatterns are completely removed after a certain etching time, and thus the Ge SWSs are overall etched without the etch mask at the longer etching time (i.e., >10 min). As the etching time was increased from 5 to 15 min, the average etch rate of tapered cone Ge SWSs was reduced from ~83 to ~46.7 nm/min while their average height and volume fraction ratio were increased from 415±115 and ~0.36 to 700±165 nm and ~0.47, respectively. The reflectance is strongly affected by the height of Ge SWSs as can be seen in (iv) of Fig. 5(a). The Ge SWS etched for 15 min, which had the highest height, exhibited the relatively low reflectance below ~10% over a wide wavelength range of 350-1800 nm, resulting in an average reflectance of 4.6%. It is noticeable that the tapered cone SWSs with taller nanopillars can yield a more gradual refractive index distribution from air to the semiconductor without any abrupt change at the interface of air/SWSs to suppress efficiently the surface reflection as mentioned above. To investigate the effect of the reflectance spectrum of the fabricated Ge SWSs on the solar cell performance, the solar weighted reflectance (R_{SWR}), i.e., the ratio of the usable photons reflected to the total usable photons, can be estimated by normalizing the reflectance spectrum with the internal quantum efficiency (IQE) spectrum of a solar cell and the terrestrial air mass 1.5 global (AM1.5g) spectrum integrated over a wavelength range of 350-1800 nm, as formally defined by Redfield [34]. The R_{SWR} is given by

$$R_{SWR} = \frac{\int R(\lambda)F(\lambda)Q_i(\lambda)d\lambda}{\int F(\lambda)Q_i(\lambda)d\lambda} \quad (1)$$

where $F(\lambda)$ is the light flux density (in photons per second per unit area, i.e., AM1.5g), $R(\lambda)$ is the surface reflectance, and $Q_i(\lambda)$ is the IQE spectrum. The IQE spectrum of the experimentally reported Ge stand-alone solar cell structure was used in this calculation [7]. For the Ge SWSs, the estimated R_{SWR} values were 12.6, 6.7, and 3.6% at etching times of 5, 10, and 15 min, respectively. At 15 min, this R_{SWR} value was lower than that of the thin film ARCs consisted of ZnS and MgF_2 (e.g., R_{SWR}~11.7% at wavelengths of 350-1800 nm for the measured reflectance) as reported in the previous work [7]. Thus, the proper selection of etching parameters can make the desirable antireflective Ge SWS by controlling the etch rate of Ge and its etch selectivity over Au nanomask patterns. Figure 5(b) shows the influence of the height of Ge SWSs on the reflectance as a function of wavelength. The three-dimensional

#155555 - $15.00 USD Received 28 Sep 2011; revised 13 Nov 2011; accepted 23 Nov 2011; published 9 Dec 2011

simulation model with a cone-shaped structure used in this calculation is shown in the inset of Fig. 5(b). We assumed that the period and bottom diameter of Ge SWSs were 250 nm and 200 nm, respectively. As the height of SWSs is increased, the overall reflectance is reduced, showing a similar trend with the experimental data. In particular, for Ge SWSs with heights above 600 nm, the reflectance is lower than 5% over a wide wavelength region of 350-1800 nm, which indicates that the low reflectance is achieved almost independent of wavelength. Figure 5(c) shows the electric field intensity distribution of the cone-shaped Ge SWS with a height of 700 nm at a wavelength of 1000 nm at normal incidence. There exists a larger electric field in the Ge compared to that with a truncated cone shape and low height, which is shown in Fig. 2(c). This is attributed to the Ge SWS with tapered and higher conical nanopillars.

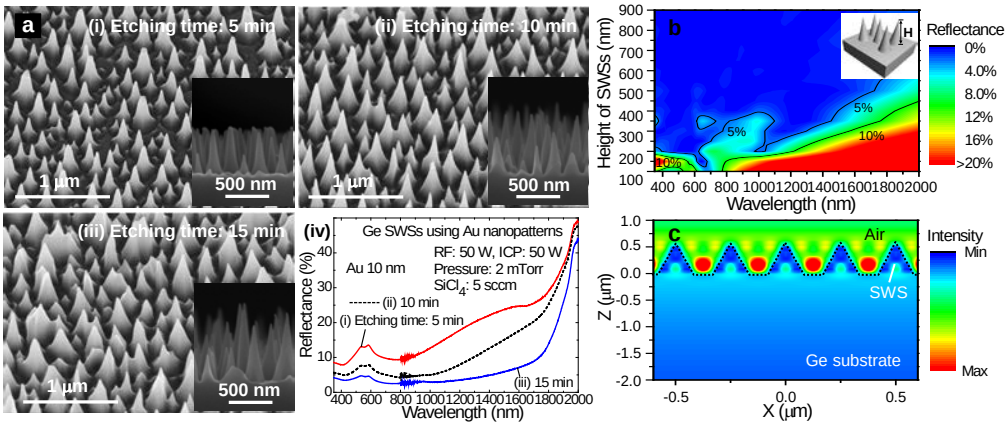

Fig. 5. (a) SEM images of the etched Ge SWSs at etching times of (i) 5 min, (ii) 10 min, and (iii) 15 min using the Au nanopatterns, (b) contour plot of calculated reflectance spectra of the Ge SWS with the tapered conical nanopillar shape as function of its height, and (c) electric field intensity distribution of the Ge SWS at a wavelength of 1000 nm at normal incidence. The measured reflectance spectra of the corresponding structures are shown in (iv) of (a). The three-dimensional simulation model with a cone-shaped structure used in this calculation is shown in the inset of (b).

For omnidirectional antireflection properties of the Ge SWSs, the incident angle (θ_i) of the linearly polarized light was varied from 15 to 85°. Figure 6(a) shows the measured reflectance of the optimized Ge SWS at 15 min of etching time under different angles of the incident light for a wavelength of 633 nm. For the incident angles of θ_i = 15-70°, the reflectance remained below 2.5% and then it significantly increased up to ~8.8% at θ_i = 85°. However, these values were much lower than that of the Ge substrate (i.e., ~47.7% at λ~633 nm) at near-normal incidence. The contour plot of calculated angle dependent reflectance spectra of the corresponding structure in Fig. 5(b) is shown in Fig. 6(b). The period, height, and bottom diameter of Ge SWSs were assumed to be 250, 700, and 200 nm, respectively. The calculated reflectance depends strongly on the incident angle over a wide wavelength region of 350-1800 nm, especially at incident angles above θ_i = 70°. However, the reflectance remains roughly below 20% at wavelengths of 350-1400 nm at incident angles less than θ_i = 70°. At wavelengths around 633 nm, the reflectance decreases up to θ_i = 50° and it abruptly increases up to θ_i = 85°. Although there are some differences between the experimentally measured and theoretically calculated results, a similar overall trend is observed. Figure 6(c) shows the photograph images of (i) Ge substrate and (ii) optimized Ge SWS for the samples (left) and the lower-magnified 30°-tilted side-view SEM image of (ii) (right). The surface of the Ge SWS clearly appeared to be dark black due to its low surface reflectivity in comparison with

#155555 - $15.00 USD Received 28 Sep 2011; revised 13 Nov 2011; accepted 23 Nov 2011; published 9 Dec 2011

the Ge substrate. As shown in the SEM image of Fig. 6(c), it can be observed that the taller and tapered cone SWS is uniformly formed on the Ge substrate over a large area.

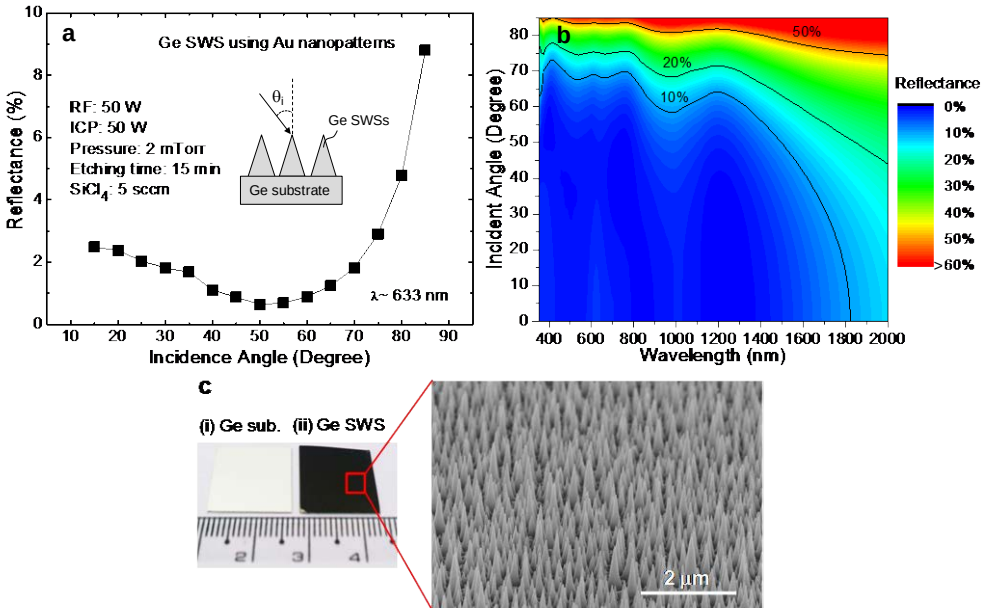

Fig. 6. (a) Measured reflectance of the optimized Ge SWS at 15 min of etching time under different angles of the incident light for a wavelength of 633 nm, (b) contour plot of calculated angle dependent reflectance spectra of the optimized Ge SWS, and (c) photograph images of (i) Ge substrate and (ii) optimized Ge SWS for the samples (left) and the lower-magnified 30°-tilted side view SEM image of (ii) (right).

4. Conclusion

To reduce the surface reflectivity of Ge for photovoltaic cell applications, the Ge SWSs were fabricated on Ge substrates using the thermally dewetted Au nanomask patterns by the ICP dry etching and their reflection properties were investigated in terms of etching parameters, together with theoretical analysis using RCWA method in the wide ranges of wavelengths and incident angles. The desirable Au nanoparticles as the etch mask were obtained after RTA of the 10 nm Au film at 450 °C for 2 min. The Ge SWSs with taller and tapered cone nanopillars significantly reduced the reflectance compared to the samples with the truncated cone shape and low height as well as the Ge substrate due to the linearly graded change in refractive index profile between air and Ge substrate via Ge SWSs. The optimized Ge SWS with the average height of 700 ± 165 nm and tapered cone shape, which was etched with 50 RF power, 50 W additional ICP power at 2 mTorr for 15 min in 5 sccm $SiCl_4$ plasma, which leaded to the reduced reflectance of <~10% over a wide wavelength range of 350-1800 nm, exhibiting the average reflectance of 4.6% and R_{SWR} value of 3.6%. Furthermore, its angle-dependent reflectance values of <8.8% were maintained at θ_i = 15–85° for a wavelength of 633 nm. The measured reflectance results of the Ge SWSs indicated similar trends to the calculated data. From these results, the broadband and omnidirectional antireflective Ge SWSs are very promising for high-performance Ge photovoltaic cell applications.

Acknowledgments

This research was supported by Basic Science Research Program through the National Research Foundation of Korea (NRF) funded by the Ministry of Education, Science and Technology (No. 2011-0003857 and No. 2010-0025071).

#155555 - $15.00 USD Received 28 Sep 2011; revised 13 Nov 2011; accepted 23 Nov 2011; published 9 Dec 2011